Atmospheric Effects on InSAR Measurements in Southern China and Australia: A Comparative Study

X. L. Ding[a, *], L. Ge[b], Z. W. Li[a], C. Rizos[b]

[a]Dept. of Land Surveying and Geo-Informatics, Hong Kong Polytechnic University, Hung Hom, Hong Kong, China - (lsxlding, zhiwei.li)@polyu.edu.hk
[b]School of Surveying and Spatial Information Systems, University of New South Wales, Sydney, NSW 2052, Australia - (l.ge, c.rizos)@unsw.edu.au

KEY WORDS: InSAR, Radon, Gaussianity, Bispectrum, Power spectrum

ABSTRACT:

Satellite synthetic aperture radar (SAR) signals are often seriously contaminated by atmospheric delays. The state of the atmosphere, especially the atmospheric water vapor, varies significantly both in space and with time. It is necessary to understand the characteristics of the atmospheric variations in order to devise appropriate means for the mitigation of the effects.

We use interferograms generated from some ERS tandem pairs covering Hong Kong, Shanghai of southern China and New South Wales of Australia to study the characteristics of the atmospheric effects in these areas. The anisotropy and Gaussianity of the atmospheric effects are first examined with the method of Radon transform and Hinich test and then compared in terms of different regions and climate patterns. The spectral features of the atmospheric effects are then analyzed with the method of Fast Fourier Transform (FFT) and power spectrum. The implication of the results on practical Interferometric SAR (InSAR) measurements, especially on the modeling and correction of the atmospheric effects are examined.

1 Introduction

Repeat-pass InSAR measurements can be significantly affected by the atmosphere (e.g., Massonnet and Feijl, 1995; Rosen et al., 1996; Tarayre and Massonnet, 1996; Zebker et al., 1997). It is useful to characterize the effects for different regions due to the highly variable nature of the effects in place and time. Beside enabling us to understanding the effect better, such studies will also offer useful results for the modeling and mitigaton of the results. In addition, the unprecedented spatial resolution of InSAR also makes it a useful too to study the atmosphere.

This paper will first generate a number of differential SAR interferograms, covering Shanghai, Hong Kong of southern China and New South Wales of Australia that reveals the atmospheric signals in the regions. The atmospheric signals are then studied comparatively for the different regions to determine such parameters of the signals as isotropy, Gaussianity and spectral features. Finally the implications of the results on modeling and mitigating the atmospheric effects on InSAR measurements are discussed.

2 Extraction of Atmospheric Signals from SAR Interferograms

A SAR interferogram generated by complex conjugate multiplication of two SAR images is a superposition of topographic information, surface deformation and atmospheric propagation delay variations between the two acquisitions, and noise (e.g., Tarayre and Massonnet, 1996; Hanssen et al., 1999; Li et al., 2003). The contribution from the topography can be removed by using a reference elevation model. That from the surface deformation can be neglected or removed if the deformation of the study area between the two image acquisitions is insignificant or the deformation is known. Besides, multi-looking operation and careful interferometric processing are also needed to suppress the noise. The atmospheric signatures can then be obtained by removing the topographic and deformation terms (Hansen et al., 1999).

We choose a tandem pair covering Shanghai, Hong Kong and New South Wales respectively in this study (see Table 1). It is safe to assume that there is no ground deformation phase in the SAR interferograms over such a short time interval. The topographic phases are removed based on external DEMs. For the Shanghai study region, the SRTM 3 arc-second DEM is used. Its accuracy is about 10m and it can potentially introduce a phase error of less than 0.05 cycles for an ambiguity height of 216 m (See Table 1). For Hong Kong region, a DEM from the Lands Department of the Hong Kong Government with an accuracy of about 10 m is used. It can cause a phase error of about 0.1 cycles. For the New South Wales region, the accuracy of the DEM is about 15 m and the phase error caused is less than 0.1 cycles. Therefore, for the three interferograms, the phase errors from DEM errors are negligible.

Precise ERS1 and ERS2 orbits from The Delft University of Technology are used in the processing to reduce errors from co-registration and flat earth phase removing (Scharroo et al., 1998). To suppress noise, the SAR images are processed by multi-looking operation with 10 pixels in azimuth and 2 pixels in range directions to get a final resolution of about 40 m by 40 m. Since the residue satellite orbit error and ionosphere will possibly introduce a linear phase ramp in interferogram (Tarayre and Massonnet, 1996; Hanssen, 1998), careful baseline refining and linear phase ramp removing procedures are also included in the interferometric processing (Atlantis, 2003). The differential interferograms and differential atmospheric delay signals in mm (mapped from unwrapped phases) for the three study regions are shown in Figure 1, 2 and 3, respectively.

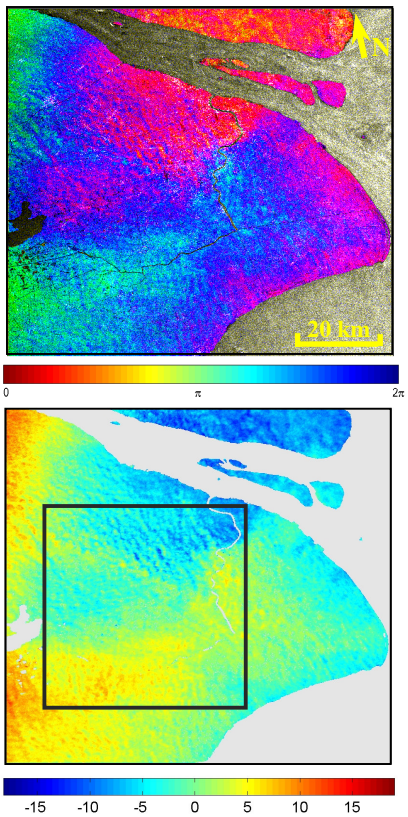

Figure 1. Differential interferogram (above) and differential atmospheric delay signals of Shanghai study region (below). A square region of 50 km × 50 km is chosen for further study.

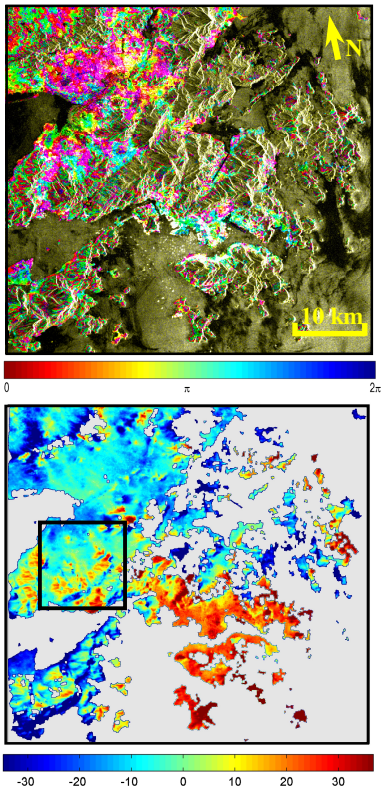

Figure 2. Differential interferogram (above) and differential atmospheric delay signals of Hong Kong study region (below). A square region of 12 km × 12 km is chosen for further study.

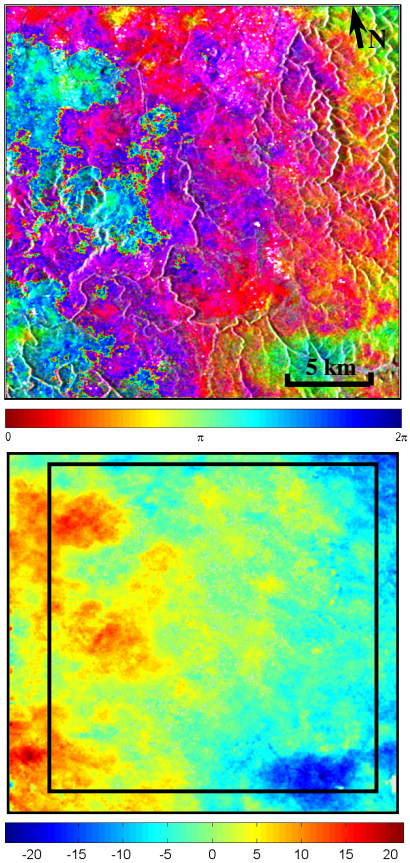

Figure 3. Differential interferogram (above) and differential atmospheric delay signals of New South Wales study region (below). A square region of 20 km × 20 km is chosen for further study.

Interferogram	Master (ERS1)	Slave (ERS2)	$B_{\perp}$ (m)	$h_{2\pi}$ (m)
Shanghai	19/02/1996	20/02/1996	-44	216
Hong Kong	18/03/1996	19/03/1996	100	95
New South Wales	29/10/1995	30/10/1995	-49	194

Table 1 Summary of the tandem pairs.

3 Anisotropy of Atmospheric Signal

3.1 The Radon Transform

Radon transform is the projection of image intensities along radial lines at a specified angle. A single Radon transform is a mapping from two dimensions to one dimension where the image intensities collapse to a profile. It is therefore a tool to investigate anisotropy in images since systematic intensity variantions in a particular direction will be significantly visible as a profile. The definition of Radon transform is (Bracewell, 1995)

$$\Re_{\theta}\{f(x,y)\}(r)=\int_{-\infty}^{\infty}\int_{-\infty}^{\infty}f(x,y)\delta(r-x\cos\theta-y\sin\theta)dxdy \quad (1)$$

where $f(x,y)$ is the image intensity, θ is the profile direction (counterclockwise from horizontal), and δ is the Dirac delta function. When applied to a discrete image d_{ij}, the Radon transform becomes

$$\Re_\theta\{d_{ij}\}_k = \sum_{l=1}^{N} d'_{kl} \quad (2)$$

where d'_{kl} is the original image rotated clockwise by an angle θ and N is the l th column of the rotated image.

3.2 Anisotropy of Atmospheric signal

To systematically examine the anisotropy of atmospheric signature, we calculate the Radon transform of each differential interferogram. In the analysis, we use a normalized version of the Radon transform (Jónsson, 2002)

$$\Re'_\theta\{d_{ij}\}_k = \Re_\theta\{d_{ij}\}_k / N \quad (3)$$

It gives the average atmospheric effect values along lines perpendicular to profile direction. The Radon transform of atmospheric signatures in the three interferograms are shown in Figures 4, 5 and 6.

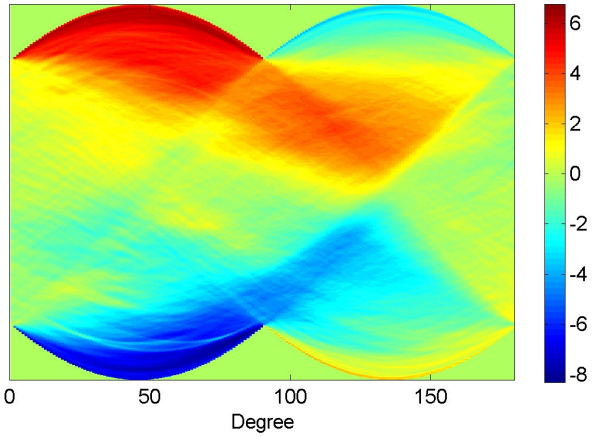

Figure 4. Radon transform of atmospheric signatures over Shanghai study region (unit: mm)

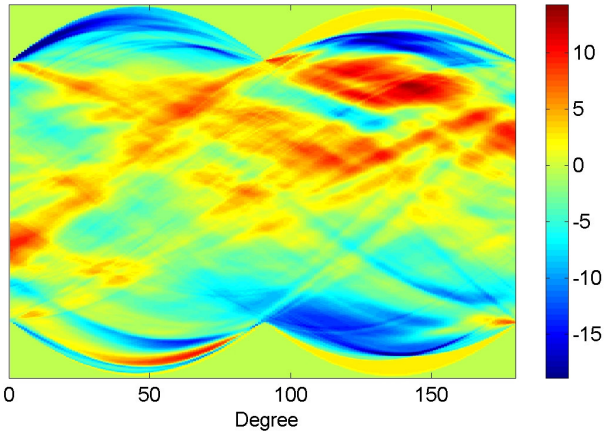

Figure 5. Radon transform of atmospheric signatures over Hong Kong study region (unit: mm)

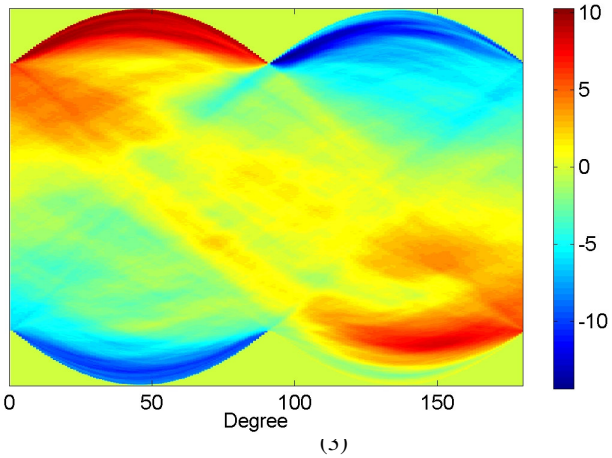

Figure 6. Radon transform of atmospheric signatures over New South Wales study region (unit: mm)

The Radon transforms of the three study regions show variable anisotropy. In the first transform, while the whole image shows a nearly opposite symmetry along the center of the profile, the extremely strong trends are visible in the two sides of the profile when the angle varies from 0 to 90 degrees. This implies that small areas of positive and negative atmospheric signals locate in the southwest and northeast corner of the original differential fields, respectively (Figure 1). The second transform (Figure 5) also shows significant anisotropy with a strong trend at about 135°. The third transform (Figure 6) shows very interesting patterns. From 0° to 90°, the values change from positive extremes to negative extremes slowly while from 91° to 180° thet change oppositely. This suggests that in all the four corners there are positive or negative phase concentrations. The original atmospheric fields (Figure 3) confirm that in the northeast and southeast corners there is a small amount of negative phases concentration while there are positive phase concentrations in the northwest and southwest corners.

Of the three transforms, the second shows much complicated variations. This may be due to the fact that the Shanghai and New South Wales regions are relatively flat, while there are several mountains in the Hong Kong region, with the highest elevation being about 1 km. The complication in mountainous region is due mainly to: (1) the vertical stratification effect or "static" effect of the troposphere (Delacourt et al., 1998; Willianms et al., 1998) related to significant topographic variations, and (2) effect of the mountains on the local weather conditions as the weather conditions can be quite different in the two sides of a mountain.

4 Non-Gaussianity of Atmospheric Signals

4.1 Statistics for Hinich Non-Gaussianity Test

If a signal is purely Gaussian, its bispectrum will be zeros. Therefore the Gaussianity of the atmospheric signals can be checked by examining the deviation of its bispectrum from zero. To this end, a consistent estimator of bispectrum from finite samples is needed. Several such estimators have been proposed in the past decades: (1) smoothing the sample bispectrum in the bifrequency domain; (2) dividing the sample into a number of segments and doing bifrequency smoothing in each segment and then averaging the piecewise smoothed bispectra; and (3) parametric method, etc. (Hinich, 1982; Lii and Rosenblatt, 1982; Nikias and Raghuveer, 1987). We will adopt the second method here.

Suppose that the sample $\{x(0), x(1), \cdots, x(N-1)\}$ is divided into L segments of M elements each (thus, $N = LM$) and that the side for bifrequency smoothing is of length M_1, the estimated bispectrum $\hat{B}(\omega_1, \omega_2)$ is (Hinich, 1982)

$$\hat{B}(\omega_1, \omega_2) = \frac{1}{L}\sum_{i=1}^{L} b^{(i)}(m,n) \qquad (4)$$

where

$$\hat{b}^{(i)}(m,n) = \frac{1}{M_1^2}\sum_{k_1=(m-1)M_1}^{mM_1-1}\sum_{k_2=(n-1)M_1}^{nM_1-1} F^{(i)}(k_1,k_2) \ ,$$

$$F^{(i)}(k_1,k_2) = \frac{1}{M} X^{(i)}(\omega_{k_1}) X^{(i)}(\omega_{k_2}) X^{(i)*}(\omega_{k_1+k_2}) \text{, and}$$

$$X^{(i)}(\omega_k) = \sum_{t=0}^{M-1} x^{(i)}(t)\exp(-j\omega_k t) \cdot$$

The statistics for non-Gaussianity test is (Hinich and Wilson, 1990)

$$TCH = 2\Delta^2{}_N N \sum_{(j,k)} \left|\hat{B}(\omega_j,\omega_k) - B(\omega_j,\omega_k)\right|^2 \Big/ \hat{S}(\omega_j)\hat{S}(\omega_k)\hat{S}(\omega_j+\omega_k) \qquad (5)$$

where $\Delta_N = LM_1/N = M_1/M$, and $\hat{S}(\omega)$ is the estimate of power spectra. If $\Delta_N \cong 1/\sqrt{N}$, TCH is an approximate Chi-square distribution with a degree of freedom of $2P$, where $P = (1/4\Delta_N)^2$.

4.2 Non-Gaussianity of Atmospheric Signals

The null hypothesis for the test is: the atmospheric signatures in a SAR interferogram are Gaussian. Under the null hypothesis, $B(\omega_1, \omega_2) \equiv 0$ for all bifrequency pairs, and thus TCH is approximately $\chi^2_{2P}(0)$. The α -level test is to reject null hypothesis if $TCH > T_\alpha$, where $\alpha = \Pr\{\chi^0_{2P} > T_\alpha\}$.

To satisfy the relationship of $\Delta_N \cong 1/\sqrt{N}$ and to conduct more detailed tests, we divide each interferogram into a number of pieces along the azimuth direction and in each piece a test is carried out. The number of tests, i.e., the number of pieces, and the test results for each of the study regions are listed in Table 2. Also shown are parameters used in bispectrum estimations for each study region.

Interfero.	Number of tests	Parameters used in Bispectrum estimation			Test Results	
		M	L	M_1	Gauss.	Non-Gauss.
Shanghai	50	1250	25	7	0	50
Hong Kong	25	300	12	5	0	25
New South Wales	25	500	20	5	0	25

Table 2. Details of Hinich Non-Gaussianity tests.

The Hinich non-Gaussianity tests show that for all the study regions the differential atmospheric signals show significant non-Gaussianity. This contradicts to assumptions made by some authors that the atmospheric signals are Gaussian (Ferretti, et al., 1999 and Yue, et al., 2002). The atmospheric effect on InSAR measurements and parameter estimation are, however, subject to further study.

5 Spectral Analysis of Atmospheric Signals

The mean differential atmospheric delays in each of the study areas are calculated and removed from the unwrapped interferograms. A 2D Fast Fourier Transform (FFT) is performed next for each of the areas and the results are squared to obtain the power spectra. The 1D rotationally averaged power spectra thus obtained are given in Figures 7, 8 and 9.

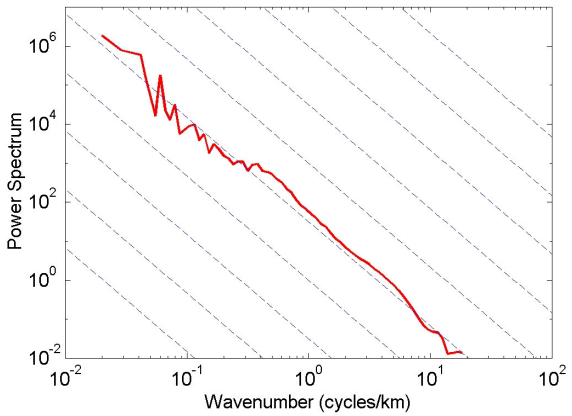

Figure 7. Power spectrum of differential atmospheric signals in the Shanghai study region. The dashed lines follow a slope of $-8/3$.

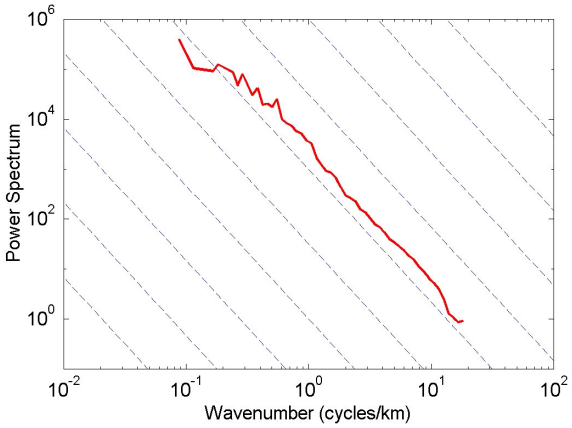

Figure 8. Power spectrum of differential atmospheric signals in the Hong Kong study region. The dashed lines follow a slope of $-8/3$.

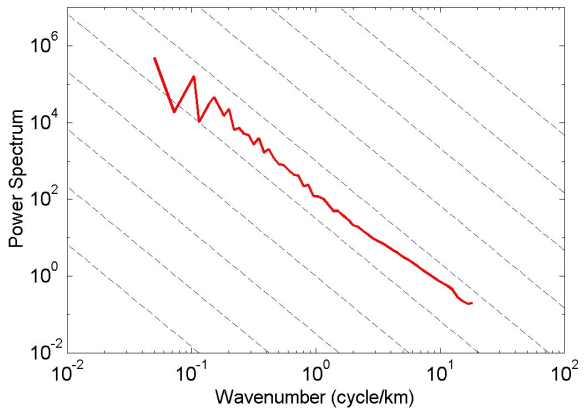

Figure 9. Power spectrum of differential atmospheric signals in the New South Wales study region. The dashed lines follow a slope of $-8/3$.

The power spectra of the differential atmospheric delays in all the three areas on the whole follow the power law, which is commonly associated with the Kolmogorov turbulence (Tatarski, 1961). The results are in good agreement with those presented by Hanssen (1998, 2001). The dashed lines in the diagrams are the $-8/3$ power law values. The power law index varies with the scales slightly, which is consistent with the turbulence behavior of such phenomena as integrated water vapor (Ruf and Beus, 1997), and the wet delays in radio ranging.

The power law spectral property of the atmospheric signals is very useful. For example, Ferretti et al (1999) takes advantage of the particular spectral (or frequency) characteristics to estimate the noise and atmospheric effects powers for each interferogram and based on the results develop method to combine the resulted SAR DEMs by means of a weighted average in wavelet domain instead of the simple average; Ferretti et al (2000) utilize the frequency characteristic to design filters to separate atmospheric effects from nonlinear subsidence; Williams et al. (1998) however conclude based on spectral analysis that the low-frequency (long-wavelength) components of atmospheric effects have the largest amplitude, and therefore the sparse external data, such as GPS and meteorological data, can be used to calibrate such effects; Li et al. (2004) incorporate the power law nature in designing algorithms to integrate CGPS and meteorological data for atmospheric effects mitigation.

Though in all of the areas the power spectra follow the power law, the absolute powers of differential atmospheric delays are different. Examining the power at the frequency of 1 km in Figure 7, 8, and 9, we know clearly that the power decreases in an order Hong Kong > New South Wales > Shanghai. This ranking order indicates to certain extent the severeness of the atmospheric effects in these areas. In flat areas, only the turbulent mixing process of the troposphere will affect the InSAR measurements, whilst in mountainous areas both turbulent mixing and vertical stratification will affect InSAR measurements. The effects of vertical stratification may even become dominant in areas with high mountains (Hanssen, 2001). While the Hong Kong study area is mountainous, Shanghai and New South Wales study areas are quite flat. For example, in the Shanghai study area, the standard deviation of ground variations is less than 5 m; the ground roughness of New South Wales is larger than that of Shanghai, but on the whole it is reasonably flat. Therefore it could reasonably be expected that the Hong Kong study area is more severely affected by the atmosphere than the New South Wales area and that the New South Wales area is more severely affected than the Shanghai area. However, it should be noted that the results are obtained for normal weather conditions. Under extreme conditions, such as thunderstorms and heavy showers, the results may vary.

6 Conclusions

The atmospheric effects on InSAR measurements in two areas of southern China and one area of Australia have been studied. The results show that in all the three areas the atmospheric signatures show strong anisotropy though with quite different patterns. The Hinich tests in the three areas invariably reveal that the atmospheric signatures are non-Gaussian, rather than being Gaussian as commonly assumed. Further spectral analysis shows that the approximate power law distribution holds for all the three study areas though with different strengths. Further study will focus on the impact of the results on InSAR measurements and parameter estimation.

Acknowledgements: The work presented was partially supported by grants from the Research Grants Council of the Hong Kong Special Administrative Region, China (Project No.: PolyU 5064/02E) and the Australian Research Council. The images are provided by European Space Agency under the Category 1 User project (AO-1227).

References:

Atlantis Scientific Inc., 2003. *Ev-InSAR version 3.0 User's Guide*. Atlantis Scientific Inc., Ontario, Canada, pp. 257.

Bracewell, R. N., 1995. *Two-Dimensional Imaging*. Prentice Hall, New Jersey, pp. 505-544.

Delacourt, C., Briole, P. and Achache, J., 1998. Tropospheric corrections of SAR interferograms with strong topography: application to Etna. *Geophysical Research Letter*, 25(15), pp. 2849-2852.

Ferretti, A., Prati, C. and Rocca, F., 1999. Multibaseline InSAR DEM Reconstruction: The Wavelet Approach. *IEEE Transactions on Geoscience and Remote Sensing*, 37(2), pp. 705-715.

Ferretti, A., Prati, C. and Rocca, F., 2000. Nonlinear Subsidence Rate Estimation Using Permanent Scatters in Differential SAR Interferometry. *IEEE Transactions on Geoscience and Remote Sensing*, 38(5), pp. 2202-2212.

Hanssen, R., 1998. *Atmospheric heterogeneities in ERS tandem SAR interferometry*. DEOS Report No.98.1, Delft University press, Delft, the Netherlands, 136 pp.

Hanssen, R.F., Wechwerth, T.M., Zebker, H.A., and Klees, R. 1999. High-resolution water vapor mapping from

interferometric radar measurements. *Science*, 283, pp. 1297-1299.

Hanssen, R.F., 2001. *Radar Interferometry: Data interpretation and Error Analysis*. Kluwer Academic Publishers, Dordrecht, 308 pp.

Hinich, M. J., 1982. Testing for Gaussianity and linearity of a stationary time series, *Journal of Time Series Analysis*, 3(3): pp. 169-176.

Hinich, M. J. and Wilson, G. R., 1990. Detection of Non-Gaussian Signals in Non-Gaussian Noise Using the Bispectrum, *IEEE Transactions on Acoustics, Speech and Signal Processing*, 38(7), pp. 1126-1131.

Jónsson, S., 2002. *Modeling Volcano and Earthquake Deformation From Satellite Radar Interferometric Observations*. Ph.D dissertation, Stanford University, pp. 11-49.

Li, Z.W., Ding, X.L., Liu, G.X. and Huang, C., 2003. Atmospheric Effects on InSAR Measurements - A Review. *Geomatics Research Australasia*, 79, pp. 43-58.

Li, Z.W., Ding, X.L. and Liu, G.X., 2004. Modeling Atmospheric Effects on InSAR with Meteorological and Continuous GPS Observations: Algorithms and Some Test results. *Journal of Atmospheric and Solar-Terrestrial Physics*, accepted.

Lii, K. S. and Rosenblatt, M., 1982. Deconvolution and Estimation of Transfer Function Phase and Coefficients for Nongaussian Linear Processes. *The Annals of Statistics*, 10(4), pp. 1195-1208.

Massonnet D., and Feigl, K. L., 1995. Discrimination of geophysical phenomena in satellite radar interferograms. *Geophysical Research Letters*, 22(12), pp. 1537-1540.

Nikias, C. L. and Raghuveer, M. R., 1987. Bispectrum estimation: A digital signal processing framework, *Proceedings of IEEE*, 75(7), pp. 869-891.

Rosen, P. A., Hensley, S., Zebker, H. A., Webb, F. H. and Fielding E. J., 1996. Surface deformation and coherence measurements of Kilauea Volcano, Hawaii, from SIR-C radar interferometry. *Journal of Geophysical Research*, 101(E10), pp. 23109-23125.

Ruf, C.S., and Beus, S.E., 1997. Retrieval of Tropospheric water vapor scale height from horizontal turbulence structure. *IEEE Trans. On Geoscience And Remote Sensing*, 35(2), pp. 203~211.

Scharroo, R., Visser, P. N. A. M., and Mets, G.J., 1998. Precise orbit determination and gravity field improvement for ERS satellites, *Journal of Geophysical Research*, 103(C4), pp. 8113-8127.

Tatarski, V. I., 1961. *Wave propagation in a turbulent medium*. McGraw-Hill, New York.

Tarayre, H. and Massonnet, D., 1996. Atmospheric propagation heterogeneities revealed by ERS-1, *Geophysical Research letters*, 23(9), pp. 989-992.

Williams, S., Bock, Y. and Fang, P., 1998. Integrated satellite interferometry: Tropospheric noise, GPS estimates and implications for interferometric synthetic aperture radar product. *Journal of Geophysical Research*, 103(B11), pp. 27051-27068.

Yue, H.Y., Guo, H.D., Wang, C.L., Liao, J.J. and Yan, F.L., 2002. Multi-temporal InSAR data fusion in wavelet domain. *Journal of Remote Sensing*, 6(6), pp., 501-506.

Zebker, H. A., Rosen, P. A. and Hensley, S., 1997. Atmospheric effects in interferometric synthetic aperture radar surface deformation and topographic maps. *Journal of Geophysical Research*, 102(B4), pp. 7547-7563.